

## First-row transition metal dichalcogenide catalysts for hydrogen evolution reaction†

Cite this: *Energy Environ. Sci.*, 2013, **6**, 3553

Desheng Kong,<sup>a</sup> Judy J. Cha,<sup>a</sup> Haotian Wang,<sup>b</sup> Hye Ryoung Lee<sup>c</sup> and Yi Cui<sup>\*ad</sup>

Received 17th July 2013  
Accepted 9th September 2013

DOI: 10.1039/c3ee42413h

www.rsc.org/ees

A group of first-row transition metal dichalcogenides ( $\text{ME}_2$ ,  $\text{M} = \text{Fe}$ ,  $\text{Co}$ ,  $\text{Ni}$ ;  $\text{E} = \text{S}$ ,  $\text{Se}$ ) are introduced as non-precious HER catalysts in an acidic electrolyte. They exhibit excellent catalytic activity especially in their nanoparticle form. These compounds expand and enrich the family of high performance HER catalysts.

The efficient generation of hydrogen through the electrochemical reduction of water is a key component of many clean energy technologies.<sup>1–4</sup> State-of-the-art hydrogen evolution reaction (HER) catalysts contain noble metals such as Pt with superior activity,<sup>5–7</sup> however these catalysts are likely to be unsuitable for large scale hydrogen production. Accordingly, abundant nickel based alloys are often commercially used as HER catalysts functioning in alkaline electrolytes.<sup>8–11</sup> However, these metal alloy catalysts are not stable in acid and therefore incompatible with proton exchange membrane based electrolysis units, which are very compact and have the potential to lower the overall capital cost.<sup>12</sup> Research efforts have therefore been directed to search for stable HER catalysts in acidic electrolytes with a few successful examples as  $\text{MoS}_2$ ,<sup>13–20</sup> amorphous  $\text{MoS}_x$ ,<sup>21–23</sup>  $\text{MoSe}_2$ ,<sup>24,25</sup>  $\text{WSe}_2$ ,<sup>25</sup>  $\text{MoB}$ ,<sup>26</sup>  $\text{Mo}_2\text{C}$ ,<sup>27</sup>  $\text{NiMoN}_x$ <sup>28</sup> and  $\text{Ni}_2\text{P}$ .<sup>29</sup> Therefore, the identification of novel high-performance HER catalysts based on non-precious materials is very attractive.

## Broader context

With the increasing interest in using hydrogen as a sustainable and carbon-free energy carrier, there is a great need to explore and optimize new catalysts suitable for electrochemical water reduction. The scale of global energy demand calls for such hydrogen evolution reaction (HER) catalysts to be fabricated from non-precious materials. In this communication, we have identified a group of HER catalysts from first-row transition metal dichalcogenides with a pyrite or marcasite structure. Our systematic electrochemical studies reveal their high activity towards the HER in an acidic electrolyte. These materials effectively enrich the family of hydrogen-producing catalysts, which may find uses in solar-fuel devices and proton exchange membrane based water electrolysis units.

In this study, we introduce a group of highly active HER catalysts from first-row transition metal dichalcogenides. These metal dichalcogenides have been previously used as catalysts for oxygen reduction reactions (ORR) in acidic media,<sup>30–32</sup> however their catalytic activity towards HER has not been identified. These compounds are among the most active electrocatalysts based on non-noble materials, which expand and enrich the family of materials suitable as efficient HER catalysts.

In biological systems, the formation of molecular hydrogen is catalyzed by metalloenzymes such as hydrogenase and nitrogenase, which contain only non-precious, transition metals ( $\text{Fe}$ ,  $\text{Ni}$  and  $\text{Mo}$ ), with their catalytic activity comparing favorably to Pt.<sup>33–35</sup> Recently, the edge sites of molybdenum disulfide ( $\text{MoS}_2$ ), which resemble the active centre of nitrogenase, have been studied as a promising electrocatalyst for the HER.<sup>13–15,17,23,36</sup> A similar structural analogy can be made for the structure of the active centre of hydrogenase, which features an Fe site with five permanent ligands in a distorted octahedral ligation shell (Fig. S1†).<sup>33,34,37</sup> By extensively exploring the structures and properties of inorganic crystals, we have identified first-row transition metal dichalcogenides ( $\text{ME}_2$ ,  $\text{M} = \text{Fe}$ ,  $\text{Co}$ ,  $\text{Ni}$ ;  $\text{E} = \text{S}$ ,  $\text{Se}$ ) which exhibit comparable structures as potential catalysts for HER. These  $\text{ME}_2$  compounds share the pyrite (Fig. 1a) or related marcasite structure (Fig. 1b), in which the metal atoms

<sup>a</sup>Department of Materials Science and Engineering, Stanford University, Stanford, CA 94305, USA. E-mail: yicui@stanford.edu; Tel: +1-650-723-4613

<sup>b</sup>Department of Applied Physics, Stanford University, Stanford, CA 94305, USA

<sup>c</sup>Department of Electrical Engineering, Stanford University, Stanford, CA 94305, USA

<sup>d</sup>Stanford Institute for Materials and Energy Sciences, SLAC National Accelerator Laboratory, 2575 Sand Hill Road, Menlo Park, California 94025, USA

† Electronic supplementary information (ESI) available: experimental details; active sites of three classes of hydrogenases (Fig. S1); schematic of the synthesis setup (Fig. S2); overview SEM images of the film morphology (Fig. S3); additional characterization (Fig. S4–12, S15); schematic of density-of-states (DOS) of transitional metal dichalcogenides (Fig. S13); additional stability tests (Fig. S14); coordination numbers for metal cations on low-index surfaces of  $\text{FeS}_2$  with pyrite structure (Table S1); summary of AFM measurements (Table S2); electrochemical measurements on transition metal dichalcogenide films (Table S3–11). See DOI: 10.1039/c3ee42413h

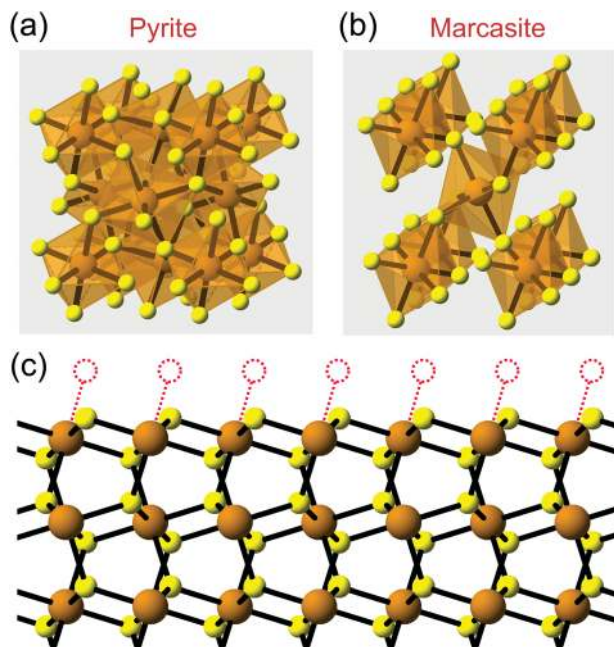


**Fig. 1** Structure of transition metal dichalcogenides in pyrite or marcasite phase. (a) Pyrite-type crystal structure, shown as  $\text{FeS}_2$  for example, in which Fe and S are displayed in orange and yellow respectively. (b) Marcasite-type crystal structures. The structural relationship between the two structures is discussed in the ESI (Fig. S8†). (c) Side-view of the stable, nonpolar pyrite (100) surface as an example of the low-index surface with under-coordinated metal cations. The (100) surface is terminated in the sequence [S–Fe–S]. The reduction in the coordination number of metal cations is common on all low-index surfaces (see Table S1†).

are octahedrally bonded to adjacent sulfur or selenium atoms. As a common structural feature, metal cations on the low-index surfaces of these dichalcogenides tend to exhibit a reduced coordination number (Table S1†). For example, the (100) surface of the pyrite structure is terminated with the stable non-polar [S–Fe–S] pattern repeated along the surface normal direction, whereas the five-fold coordinated metal cation is in a square pyramidal environment (Fig. 1c).<sup>38</sup> Note that multiple low energy planes may be present on  $\text{ME}_2$  films or nanoparticles to drive the catalytic reaction, which also varies between the synthesis techniques largely dependant on a S/Se rich or poor environment during the synthesis.<sup>39</sup> For  $\text{ME}_2$ , the ligand number and symmetry of some under-coordinated surface cations bear certain similarities to the active centre of hydrogenase, which suggests they may be interesting candidate materials for HER.

We developed a facile process to grow polycrystalline dichalcogenide films on diverse substrates, which has been used to grow  $\text{MoS}_2$  with vertically aligned layers.<sup>24</sup> These films are formed by converting e-beam evaporated metal thin-films into their corresponding dichalcogenides with a sulfurization/selenization reaction. The synthesis is performed in a horizontal tube furnace, in which elemental sulfur/selenium powders are used as the precursors (see Experimental details†). Diverse dichalcogenide films with a pyrite/marcasite structure were synthesized based on this process, as confirmed by the systematic structural and compositional characterizations (Fig. S4–S12†). For example, Fig. 2a shows a scanning electron

microscopy (SEM) image of a  $\text{CoSe}_2$  film grown on a mirror polished glassy carbon substrate, revealing individual grains in the dimension of several hundred nanometers. In Fig. 2b, a corresponding transmission electron microscopy (TEM) image reveals the grains are densely packed to form a polycrystalline film. A magnified TEM image of an individual grain (inset of Fig. 2b) shows sharp lattice fringes, confirming its crystalline quality. Selected area electron diffraction over multiple grains yields a ring pattern well indexed as  $\text{CoSe}_2$  in pyrite structure (Fig. S4†). Fig. 2c presents Raman spectra of the films grown on oxidized silicon and glassy carbon substrates showing spectral features consistent with the characteristic peak of  $\text{CoSe}_2$  at  $190\text{ cm}^{-1}$ ,<sup>40</sup> suggesting the film quality is less sensitive to the choice of the substrates. The similar synthesis procedure was used to grow all the  $\text{ME}_2$  films, reported in this communication.

The activity of the  $\text{ME}_2$  for the HER is studied based on thin films grown on mirror-polished glassy carbon substrates. Glassy carbon is the ideal substrate due to its negligible HER activity within the measurement voltage range. Electrochemical studies were performed in a  $0.5\text{ M H}_2\text{SO}_4$  solution using a typical three-electrode cell set-up (see Experimental details†). We present the surface-area-normalized current density,  $j_s$ , corrected by the specific surface area based on atomic force microscopy (AFM) topology (Table S2†), as a function of the potential in Fig. 3a and c. According to the polarization curves ( $j_s$  vs.  $E$ ), it is evident that these dichalcogenides exhibit excellent activity, achieving a cathodic current density of  $4\text{ mA cm}^{-2}$  that ranges from 190 mV to 270 mV. The corresponding Tafel plots ( $\log j_s$  vs.  $E$ ), shown in Fig. 3b and d, reveal different Tafel slopes among these dichalcogenides, which are summarized in Fig. 3e. A small Tafel slope is desirable to drive a large catalytic current density at low over-potential and non-precious HER catalysts usually exhibit Tafel slopes ranging from 40 to 120 mV per dec.<sup>13–20,23–27,29</sup> As shown in

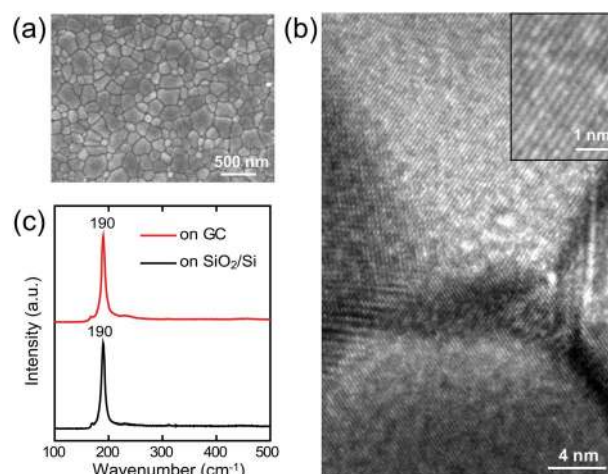


**Fig. 2** Characterization of transition metal dichalcogenide films. (a) SEM image of a  $\text{CoSe}_2$  film with densely packed grains. (b) TEM image of a few grains in the film. Inset: high-resolution TEM image of individual grain showing lattice fringes that confirm the film is crystalline in nature. (c) Raman spectra from  $\text{CoSe}_2$  films grown on glassy carbon (GC) and oxidized silicon ( $300\text{ nm SiO}_2/\text{Si}$ ) substrates, respectively. The peak at  $190\text{ cm}^{-1}$  corresponds to the characteristic active mode for  $\text{CoSe}_2$  with pyrite structure.<sup>12</sup>

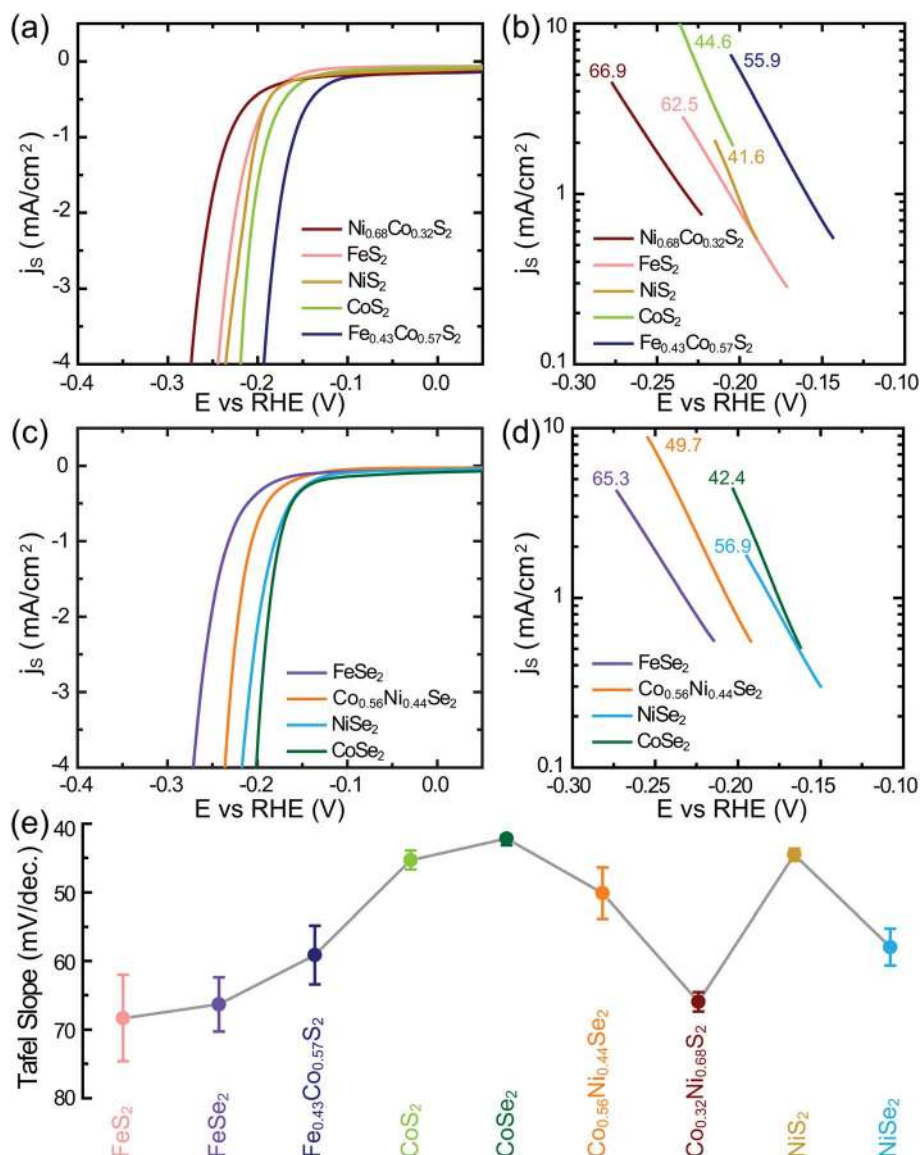


**Fig. 3** Electrochemical measurements of transition metal dichalcogenide films grown on glassy carbon electrodes. (a) Polarization curves of transition metal disulfides, in which surface-area-normalized current density,  $j_s$ , is plotted against the potential. (b) Corresponding Tafel plots ( $\log j_s$  vs.  $E$ ) of transition metal disulfides. Tafel slopes in the unit of mV per dec. are displayed. (c) and (d) Polarization curves of transition metal diselenides and the corresponding Tafel plots. (e) Summary of Tafel slopes of transition metal dichalcogenide films.

Fig. 3e, the Tafel slopes of  $\text{ME}_2$  are in the range 40–70 mV per dec. showing relatively fast kinetics to drive the HER among these compounds. Optimal Tafel slopes of  $\sim 40$  mV per dec. are achieved in a few compounds including  $\text{CoS}_2$ ,  $\text{CoSe}_2$  and  $\text{NiS}_2$ .

For electrocatalysts, it is the reactive states near the Fermi level that are most responsible for the catalytic activity.<sup>41</sup> In these metal dichalcogenides,  $d$ -electron filling in  $e_g$  orbitals contributes primarily to the density of states in the conduction band (Fig. S13†).<sup>42–44</sup> It is interesting to note that the best activity among  $\text{ME}_2$  is achieved using  $\text{CoSe}_2$  and  $\text{Fe}_{0.43}\text{Co}_{0.57}\text{S}_2$  when the  $e_g$  band is partially filled.<sup>42,45</sup> The excellent activity of  $\text{CoSe}_2$  and  $\text{Fe}_{0.43}\text{Co}_{0.57}\text{S}_2$  is likely linked with their unique electronic structures.

Stability is an important criterion in the development of electrocatalysts. We evaluated the stability of all metal

dichalcogenide films measured in this study. The tests were performed by taking continuous cyclic voltammograms at an accelerated scanning rate of  $50 \text{ mV s}^{-1}$  for 1000 cycles.<sup>15</sup> We identified several durable HER catalysts through this test, where the polarization curve after 1000 cycles overlays almost exactly with the initial one (see Fig. 4). The exceptional durability promises the practical applications of these catalysts over the long term. In contrast, a loss in cathodic current density through continuous potential cycles was observed for several dichalcogenide films including  $\text{FeSe}_2$ ,  $\text{NiS}_2$  and  $\text{Co}_{0.68}\text{Ni}_{0.32}\text{S}_2$  (see Fig. S14†).

Inorganic catalysts in a nanoparticle form are usually employed in HER electrodes to increase the exposed catalytic sites. Herein, we prepared  $\text{CoSe}_2$  nanoparticles by templating commercial carbon black nanoparticles (from Alfa Aesar). These



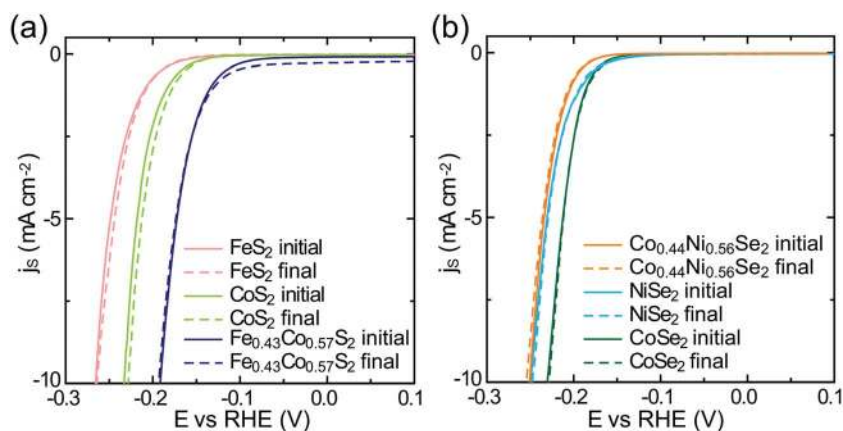


**Fig. 4** Stability tests for several transition metal disulfide (a) and diselenide (b) films, in which the polarization curves before and after 1000 potential cycles are displayed.

carbon black nanoparticles are conformally coated with a Co layer as the precursor, by adopting DC magnetosputtering conditions previously used to prepare CuO/Co core-shell nanowires.<sup>46</sup> Subsequently, these particles are selenized in the tube furnace (see Experimental details†). Fig. 5a presents a

typical SEM image of the catalyst nanoparticles assembled on the glassy carbon electrode. The nanoparticle assembly exhibits a mesoporous morphology readily used as a catalyst. The energy-dispersive X-ray spectroscopy (EDX) spectrum reveals the presence of C, Co and Se elements in these nanoparticles

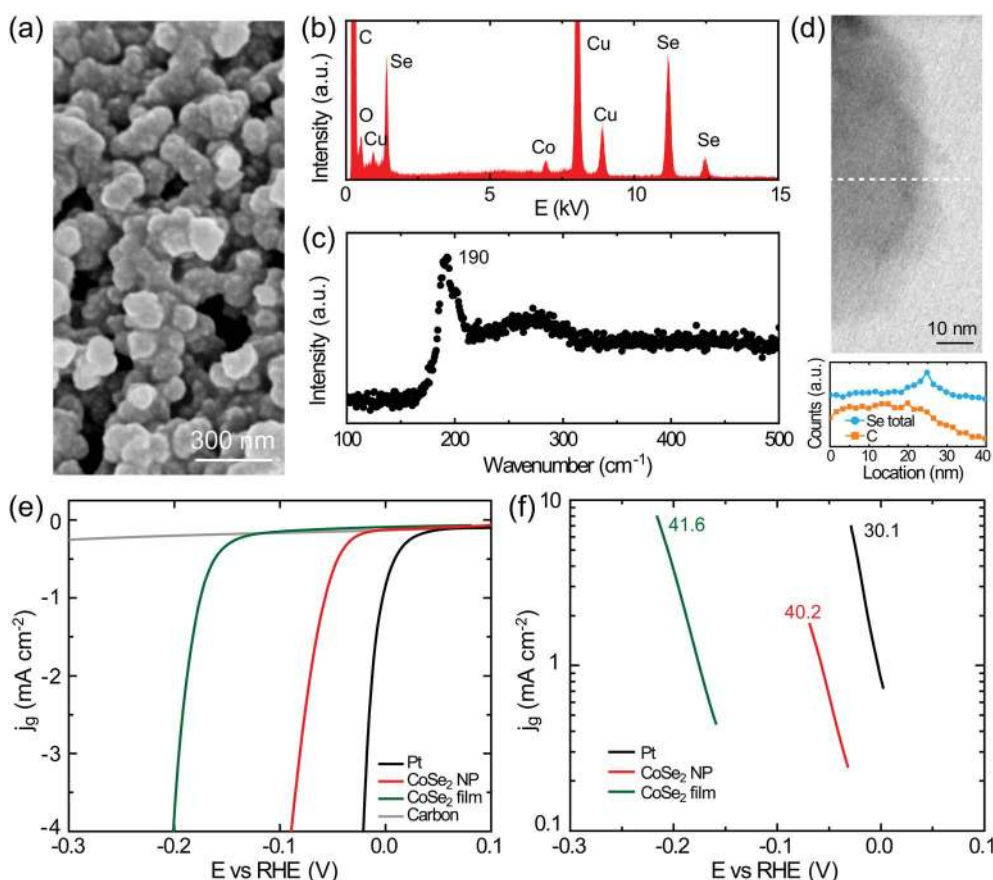


**Fig. 5** Characterization and electrochemical measurements of C/CoSe<sub>2</sub> core-shell nanoparticles. (a) SEM image of C/CoSe<sub>2</sub> core-shell nanoparticles assembled on a glassy carbon substrate. (b) EDX spectra acquired in TEM reveal the chemical composition of the nanoparticle containing Co, Se and C. The Cu peaks come from the TEM grid. (c) Raman spectrum showing the characteristic active mode at 190 cm<sup>-1</sup> for CoSe<sub>2</sub> in pyrite phase.<sup>12</sup> (d) TEM image and EDX elemental line scan of C and Se of a single nanoparticle (corresponding to the dashed line in the image). (e) Polarization curves of C/CoSe<sub>2</sub> core-shell nanoparticles, CoSe<sub>2</sub> film, Pt and carbon black nanoparticles. The nanoparticle exhibits a largely enhanced activity as compared with the thin film, approaching the performance of a state-of-art Pt catalyst. (f) Corresponding Tafel plots in which Tafel slopes in the unit of mV per dec. are displayed.

(Fig. 5b), suggesting the conversion of the Co layer into corresponding selenide. In addition, Raman spectrum (Fig. 5c) collected from these nanoparticles showed the characteristic peak of CoSe<sub>2</sub> at 190 cm<sup>-1</sup>,<sup>40</sup> which confirms Co has been converted into the CoSe<sub>2</sub> phase. In Fig. 5d, normalized EDX line profiles show the even distribution of C concentration across the nanoparticle, whereas Se concentration peaks on the edge, thereby confirming the C/CoSe<sub>2</sub> core-shell structure of the nanoparticles. Additional EDX line scans reveal a certain inhomogeneity of the CoSe<sub>2</sub> shell on some nanoparticles (see Fig. S15†). We further measured the activity of the C/CoSe<sub>2</sub> nanoparticles with a mass loading of ~37 μg cm<sup>-2</sup> for the active CoSe<sub>2</sub> component. The geometric current density,  $j_g$ , of the CoSe<sub>2</sub> nanoparticle catalyst as a function of the voltage is shown in Fig. 5e. The CoSe<sub>2</sub> nanoparticle catalyst exhibits a dramatically improved activity compared with the CoSe<sub>2</sub> film; a significant  $j_g$  is achieved at very low overpotential (e.g. 4 mA cm<sup>-2</sup> at 90 mV). The overall performance of CoSe<sub>2</sub> nanoparticles is amongst the most active non-noble HER catalysts reported to date. The corresponding Tafel plot (Fig. 5f) reveals a Tafel slope of ~40 mV per dec, consistent with the value of CoSe<sub>2</sub> films. This suggests a similar surface chemistry in HER, as quite similar synthesis procedures were employed to produce these C/CoSe<sub>2</sub> core-shell nanoparticles. An exchange current density of  $3.7 \times 10^{-5}$  A cm<sup>-2</sup> was observed due to the high-surface-area catalyst structure, which is over two orders of magnitude larger than the value of  $(5.9 \pm 1.7) \times 10^{-8}$  A cm<sup>-2</sup> for CoSe<sub>2</sub> films (Table S7†). More importantly, the positive shift of onset overpotential for the HER, which drives a cathodic current of 0.5 mA cm<sup>-2</sup> at 45 mV, gives rise to the marked improvement in the overall catalytic activity. Generally, the performance of inorganic catalysts may be sensitive to the particle dimension due to variations in surface structure and electronic properties.<sup>47–49</sup> A few nanometers thick CoSe<sub>2</sub> shell likely gives rise to sufficient size confinement to enhance the activity, which needs further study.

## Conclusions

We have introduced a large family of active HER catalysts from first-row transition metal dichalcogenides, which largely expands the family of hydrogen-producing catalysts in acid electrolytes. This study exemplifies the biomimetic approach to search for new catalysts. Our study reports C/CoSe<sub>2</sub> core-shell nanoparticles which show exceptional activity among the most active HER catalysts based on non-precious materials. These nanoparticulate dichalcogenide catalysts are promising as non-precious HER catalysts for large-scale water splitting technology. Future research may involve the development of synthesis processes to grow these catalysts in a cost-effective way.

## Acknowledgements

We acknowledge the support by the Department of Energy, Office of Basic Energy Sciences, Materials Sciences and Engineering Division, under Contract DE-AC02-76-SFO0515.

## Notes and references

- 1 H. B. Gray, *Nat. Chem.*, 2009, **1**, 7.
- 2 N. S. Lewis and D. G. Nocera, *Proc. Natl. Acad. Sci. U. S. A.*, 2006, **103**, 15729–15735.
- 3 M. G. Walter, E. L. Warren, J. R. McKone, S. W. Boettcher, Q. Mi, E. A. Santori and N. S. Lewis, *Chem. Rev.*, 2010, **110**, 6446–6473.
- 4 T. R. Cook, D. K. Dogutan, S. Y. Reece, Y. Surendranath, T. S. Teets and D. G. Nocera, *Chem. Rev.*, 2010, **110**, 6474–6502.
- 5 S. Schuldiner, *J. Electrochem. Soc.*, 1959, **106**, 891–895.
- 6 J. Greeley, J. K. Nørskov, L. A. Kibler, A. M. El-Aziz and D. M. Kolb, *ChemPhysChem*, 2006, **7**, 1032–1035.
- 7 W. Sheng, H. A. Gasteiger and Y. Shao-Horn, *J. Electrochem. Soc.*, 2010, **157**, B1529–B1536.
- 8 D. E. Brown, M. N. Mahmood, A. K. Turner, S. M. Hall and P. O. Fogarty, *Int. J. Hydrogen Energy*, 1982, **7**, 405–410.
- 9 D. E. Brown, M. N. Mahmood, M. C. M. Man and A. K. Turner, *Electrochim. Acta*, 1984, **29**, 1551–1556.
- 10 I. A. Raj and K. I. Vasu, *J. Appl. Electrochem.*, 1990, **20**, 32–38.
- 11 S. Y. Reece, J. A. Hamel, K. Sung, T. D. Jarvi, A. J. Esswein, J. J. H. Pijpers and D. G. Nocera, *Science*, 2011, **334**, 645–648.
- 12 S. Kotrel and S. Bräuninger, *Industrial Electrocatalysis*, Wiley-VCH Verlag GmbH & Co. KGaA, 2008.
- 13 B. Hinnemann, P. G. Moses, J. Bonde, K. P. Jørgensen, J. H. Nielsen, S. Hørch, I. Chorkendorff and J. K. Nørskov, *J. Am. Chem. Soc.*, 2005, **127**, 5308–5309.
- 14 T. F. Jaramillo, K. P. Jørgensen, J. Bonde, J. H. Nielsen, S. Hørch and I. Chorkendorff, *Science*, 2007, **317**, 100–102.
- 15 Y. Li, H. Wang, L. Xie, Y. Liang, G. Hong and H. Dai, *J. Am. Chem. Soc.*, 2011, **133**, 7296–7299.
- 16 Z. Chen, D. Cummins, B. N. Reinecke, E. Clark, M. K. Sunkara and T. F. Jaramillo, *Nano Lett.*, 2011, **11**, 4168–4175.
- 17 J. Kibsgaard, Z. Chen, B. N. Reinecke and T. F. Jaramillo, *Nat. Mater.*, 2012, **11**, 963–969.
- 18 M. A. Lukowski, A. S. Daniel, F. Meng, A. Forticaux, L. Li and S. Jin, *J. Am. Chem. Soc.*, 2013, **135**, 10274–10277.
- 19 A. B. Laursen, S. Kegnaes, S. Dahl and I. Chorkendorff, *Energy Environ. Sci.*, 2011, **5**, 5577–5591.
- 20 D. Merki and X. Hu, *Energy Environ. Sci.*, 2011, **4**, 3878–3888.
- 21 D. Merki, S. Fierro, H. Vrubel and X. Hu, *Chem. Sci.*, 2011, **2**, 1262–1267.
- 22 H. Vrubel, D. Merki and X. Hu, *Energy Environ. Sci.*, 2011, **5**, 6136–6144.
- 23 D. Merki, H. Vrubel, L. Rovelli, S. Fierro and X. Hu, *Chem. Sci.*, 2012, **3**, 2515–2525.
- 24 D. Kong, H. Wang, J. J. Cha, M. Pasta, K. J. Koski, J. Yao and Y. Cui, *Nano Lett.*, 2013, **13**, 1341–1347.
- 25 H. Wang, D. Kong, P. Johanes, J. J. Cha, G. Zheng, K. Yan, N. Liu and Y. Cui, *Nano Lett.*, 2013, **13**, 3426–3433.
- 26 H. Vrubel and X. Hu, *Angew. Chem., Int. Ed.*, 2012, **124**, 12875–12878.
- 27 W. F. Chen, C. H. Wang, K. Sasaki, N. Marinkovic, W. Xu, J. T. Muckerman, Y. Zhu and R. R. Adzic, *Energy Environ. Sci.*, 2013, **6**, 943–951.

- 28 W.-F. Chen, K. Sasaki, C. Ma, A. I. Frenkel, N. Marinkovic, J. T. Muckerman, Y. Zhu and R. R. Adzic, *Angew. Chem., Int. Ed.*, 2012, **51**, 6131–6135.
- 29 E. J. Popczun, J. R. McKone, C. G. Read, A. J. Biacchi, A. M. Wiltout, N. S. Lewis and R. E. Schaak, *J. Am. Chem. Soc.*, 2013, **135**, 9267–9270.
- 30 Y. Feng, T. He and N. Alonso-Vante, *Electrochim. Acta*, 2009, **54**, 5252–5256.
- 31 D. Susac, L. Zhu, M. Teo, A. Sode, K. C. Wong, P. C. Wong, R. R. Parsons, D. Bizzotto, K. A. R. Mitchell and S. A. Campbell, *J. Phys. Chem. C*, 2007, **111**, 18715–18723.
- 32 L. Zhu, M. Teo, P. C. Wong, K. C. Wong, I. Narita, F. Ernst, K. A. R. Mitchell and S. A. Campbell, *Appl. Catal., A*, 2010, **386**, 157–165.
- 33 P. M. Vignais, B. Billoud and J. Meyer, *FEMS Microbiol. Rev.*, 2001, **25**, 455–501.
- 34 S. Shima, O. Pilak, S. Vogt, M. Schick, M. S. Stagni, W. Meyer-Klaucke, E. Warkentin, R. K. Thauer and U. Ermler, *Science*, 2008, **321**, 572–575.
- 35 S. C. Lee and R. H. Holm, *Proc. Natl. Acad. Sci. U. S. A.*, 2003, **100**, 3595–3600.
- 36 H. I. Karunadasa, E. Montalvo, Y. J. Sun, M. Majda, J. R. Long and C. J. Chang, *Science*, 2012, **335**, 698–702.
- 37 Y. Nicolet, C. Piras, P. Legrand, C. E. Hatchikian and J. C. Fontecilla-Camps, *Structure*, 1999, **7**, 13–23.
- 38 R. Sun, M. K. Y. Chan and G. Ceder, *Phys. Rev. B: Condens. Matter Mater. Phys.*, 2011, **83**, 235311.
- 39 D. R. Alfonso, *J. Phys. Chem. C*, 2010, **114**, 8971–8980.
- 40 E. Anastassakis, *Solid State Commun.*, 1973, **13**, 1297–1301.
- 41 J. K. Nørskov, F. Abild-Pedersen, F. Studt and T. Bligaard, *Proc. Natl. Acad. Sci. U. S. A.*, 2011, **108**, 937–943.
- 42 S. Ogawa, *J. Appl. Phys.*, 1979, **50**, 2308–2311.
- 43 J. A. Tossell, D. J. Vaughan and J. K. Burdett, *Phys. Chem. Miner.*, 1981, **7**, 177–184.
- 44 T. A. Bither, R. J. Bouchard, W. H. Cloud, P. C. Donohue and W. J. Siemons, *Inorg. Chem.*, 1968, **7**, 2208–2220.
- 45 H. S. Jarrett, W. H. Cloud, R. J. Bouchard, S. R. Butler, C. G. Frederick and J. L. Gillson, *Phys. Rev. Lett.*, 1968, **21**, 617–620.
- 46 W. Shi and N. Chopra, *ACS Appl. Mater. Interfaces*, 2012, **4**, 5590–5607.
- 47 A. T. Bell, *Science*, 2003, **299**, 1688–1691.
- 48 Y. Li and G. A. Somorjai, *Nano Lett.*, 2010, **10**, 2289–2295.
- 49 J. Kleis, J. Greeley, N. A. Romero, V. A. Morozov, H. Falsig, A. H. Larsen, J. Lu, J. J. Mortensen, M. Dułak, K. S. Thygesen, J. K. Nørskov and K. W. Jacobsen, *Catal. Lett.*, 2011, **141**, 1067–1071.